



Prediction of porosity characteristics of aluminium castings based on X-ray CT measurements

M. Weidt, R. A. Hardin, C. Garb, J. Rosc, R. Brunner & C. Beckermann

To cite this article: M. Weidt, R. A. Hardin, C. Garb, J. Rosc, R. Brunner & C. Beckermann (2018) Prediction of porosity characteristics of aluminium castings based on X-ray CT measurements, International Journal of Cast Metals Research, 31:5, 289-307, DOI: [10.1080/13640461.2018.1467105](https://doi.org/10.1080/13640461.2018.1467105)

To link to this article: <https://doi.org/10.1080/13640461.2018.1467105>



Published online: 09 May 2018.



Submit your article to this journal [↗](#)



Article views: 59



View Crossmark data [↗](#)



Prediction of porosity characteristics of aluminium castings based on X-ray CT measurements

M. Weidt^a , R. A. Hardin^b, C. Garb^c, J. Rosc^d, R. Brunner^d  and C. Beckermann^b

^aMagma Gießereitechnologie GmbH, Aachen, Germany; ^bDepartment of Mechanical and Industrial Engineering, University of Iowa, Iowa City, USA; ^cDepartment Product Engineering, Chair of Mechanical Engineering, Montanuniversität Leoben, Leoben, Austria; ^dMaterials Center Leoben Forschung GmbH, Leoben, Austria

ABSTRACT

Porosity is a main factor limiting the fatigue performance of aluminium castings. Using micro X-ray computed tomography, size and morphology characteristics of porosity distributions are analysed for material from a cast Al–8Si–3Cu–(Sr) crankcase as well as from cast Al–8Si–3Cu–(Sr), Al–7Si–0.5Cu–Mg–(Sr) and Al–7Si–0.5Cu–Mg–(Na) cylinder heads. Correlations are developed between the porosity volume percentage and mean and maximum pore sizes. Two characteristic size measures of the porosity distribution are identified: the volume weighted spherical mean diameter and the volume weighted mean envelope diameter. Both correlate linearly with the corresponding diameters of the largest pore. The pore morphology is described by a volume weighted mean sphericity. This mean sphericity and the local amount of porosity are used to predict the mean and maximum pore sizes of the porosity distributions. These correlations will find applications in integrated computational materials engineering.

ARTICLE HISTORY

Received 4 December 2017
Accepted 6 April 2018

KEYWORDS

Aluminium casting; X-ray computed tomography; microporosity; pore size distribution; sphericity

1. Introduction

The casting industry continuously strives to improve the mechanical properties of cast components. The prediction of defect size and its effect on material properties such as elongation to failure, tensile strength, and fatigue strength are some of the most pressing issues to achieve lighter and better performing cast components. Understanding these issues will improve the competitiveness of the aluminium casting industry in particular. Microporosity is a ubiquitous defect in aluminium castings. Detailed knowledge about the behaviour and development of the pore morphological features is crucial for the prediction of local fatigue properties. Understanding and predicting the effect of porosity on fatigue life is an essential link in a chain of casting design and process modelling to evaluate the in service fatigue performance of aluminium cast parts [1]. Previous works used two alternative parameters to describe the defect, which initiates the final fatigue crack. First, the maximum Feret diameter and second, the square root of the defect's projection area [2,3]. However, if a micropore constitutes the largest defect in the microstructure, it is the limiting factor for the fatigue performance of the cast part [4–9].

The physics and factors influencing porosity formation are manifold. Only recent developments in X-ray

computed tomography enabled the observation of *in situ* three-dimensional solidification with high spatial (sub micron) and temporal (seconds) resolution [10,11]. Research into the thermal solidification conditions and their impact on pore size was reported by Tiedje et al. [12]. Here, they show that the amount of the porosity as well as the morphology of the pores are predominantly controlled by the morphology of the solidifying alloy and the space available for pore growth. The flow of liquid through the semisolid mush to feed solidification shrinkage depends on the solid structure. Tiedje et al. found three characteristic zones in an AlSi7 alloy. The first is an outer zone with a high thermal gradient, exhibiting fine globular grains and therefore little porosity. The second zone is a transition characterised by elongated columnar dendrites and concomitant elongated pores created by difficult feeding conditions. The third zone has larger equiaxed grains and accompanying rounded and dispersed porosity. Whether or not, and to what extent these zones are present after solidification, varies with modification, cooling rate, composition and grain refinement.

The influence of the eutectic modification by Sr was investigated by Dinnis et al. [13]. They found a significant influence of Sr modification on the amount, distribution, and morphology of porosity in alloys with a sufficient

amount of eutectic phase. Strontium modification suppresses porosity formation in hot spots and promotes a dispersed and more uniform pore distribution and spherical morphology. The effect of Sr and Na modification was investigated by McDonald et al. [14]. In both modifications, the effect can be explained by changes in the eutectic solidification. Sodium and strontium strongly increase the eutectic grain size with presumably larger liquid pools in the late stages of solidification which cannot be fed. The effect of Na was found to be even stronger compared to Sr. These findings are supported by the research of Li et al. [15], who observed porosity mainly at eutectic grain boundaries.

Savelli et al. [16] published research on the influence of the hydrogen content of aluminium melts and the formation of porosity via micro-X-ray computed tomography. They found that the volume fraction and pore sizes increase with the hydrogen content of the melt. Moreover, they divided the porosity in two populations, characterised by the pores' sphericity. All experiments showed low sphericity pores associated with a late stage pore formation. Only experimental melts containing higher hydrogen levels showed a second population of high sphericity pores, typically denoted as 'gas porosity'. These are associated with an early and continuous formation during solidification.

Dinnis et al. [17] and Taylor et al. [18–20] found that needle/platelike Fe rich intermetallics influence the nucleation of pores depending on the Cu content of the melt. Dinnis et al. found a difference in porosity formation behaviour between alloys without and with Cu. The latter exhibit a porosity minimum at a critical Fe content of 0.4 wt-%. Wang et al. [21,22] observed pore growth around Fe rich intermetallics in recent synchrotron X-ray radiography experiments. They found pore growth dependent on both the Fe level and the time of intermetallic formation relative to pore nucleation. They concluded that β -Fe intermetallics reduce the solid/gas interfacial energy which promoted pore growth along these intermetallics. Additionally, they argued that the Fe rich intermetallics also reduce the local hydrogen diffusion capabilities by impeding the diffusion across the plates.

Numerous researchers tried to use the established knowledge to predict porosity with and without consideration of the influence of hydrogen. Lee et al. [23] and Stefanescu [24] reviewed existing porosity models. In 2007, Carlson et al. [25] presented a volume averaged model, which accounts for dissolved gas and solidification shrinkage induced microporosity. The pressure drop due to solidification and the required feeding flow through the mushy zone, as well as the diffusion controlled hydrogen contribution, were modelled. By coupling the gas species conservation equation with the feeding flow and the pressure field, Yao et al. [26] were able to show that the model of Carlson et al. can

predict gas induced porosity in A356 aluminium alloy with reasonable accuracy. However, the local amount of porosity is a necessary but not a sufficient variable in order to predict local fatigue performance. Felberbaum and Rappaz [27] investigated the mean curvature of late stage pores. In grain refined alloys they observed equiaxed pores. In non-grain refined alloys, they found elongated pores in the direction of the columnar dendrite growth and parallel to the thermal gradient. They showed that the impingement of the primary phase and the pores is mainly controlled by the volume fraction of the primary phase and secondary dendrite arm spacing. The hydrogen content was found to have only a minor influence on the pore curvature.

In this work, the characterisation of pore size distribution and pore morphology is investigated by using micro X-ray computed tomography (XCT) and a self-developed routine. This work establishes correlations between porosity, morphology and defect size and therefore between the microporosity in cast aluminium material and the fatigue performance in service. Experimental measurements of porosity are performed on material taken from two production castings. The castings are representative of typical solidification conditions in the sand and permanent mold processes. Two grain refined alloys with Sr or Na modification were cast from the Al–Si–Mg–Cu alloy system. Specimens were extracted at three different locations per casting. A total of sixty samples were scanned by micro XCT and analysed to determine their porosity volume and characteristics. Due to space limitations, analysis results from eight of these specimens from four distinct porosity levels are presented in detail. A volume weighted averaging approach is applied and two characteristic size measures are identified: (1) the volume weighted spherical mean diameter and (2) the volume weighted mean envelope diameter. By this weighting procedure, the influence of small pores and the inaccuracy of pore detection close to the resolution limit are minimised. The analysed quantities are essentially independent of the XCT scan resolution used. Details of the XCT measurements and analysis such as the suitability of the XCT radiation source, the spatial resolution needed, the required size of the scanned volume, and the data processing techniques are discussed elsewhere by Garb et al. [28]. The developed framework is the first step in an integrated computational materials engineering (ICME) approach to enable the fatigue proof design of new cast components.

2. Description of experiments

2.1. Casting procedure

Two engine components, a crankcase and cylinder head, were cast under typical industrial processing conditions. From these components, specimen material was taken to measure porosity volume and characteristics of the

pore size and morphology distribution. These castings are representative of a broad range of aluminium cast components and are subjected to a wide range of mean cooling rates from approximately 0.1 to 8 K s^{-1} between the liquidus and solidus temperature, due to the use of both permanent mold and sand mold processes. The alloys cast in this study are typical for applications in the automotive power train.

The crankcase casting, utilised for a four cylinder engine, was cast by Nematik Dillingen, Germany, using the CPS® (core package system) process [29]. The process shows advantages with respect to a high degree of automatization, constructional flexibility, a local control of the microstructure through chills and high quality castings at high volumes of production. In the CPS process, a core package is assembled on an automated assembly line. A construction tray is moving through the process, and cores are simultaneously shot and introduced into the process. After the core package is assembled, it is filled automatically from a continuous cast alloy distribution system. Directly after filling, the casting is 'rolled over' by a rotation of 180° to enable a natural solidification from the bottom to the feeder. The castings for this work were extracted from the production line process. The crankcase casting is made from an Al-Ti-B grain refined and Sr modified Al-8Si-3Cu recycled alloy. Three locations in the casting were selected for the analysis: (1) at the bridge (between two chills forming the cylinder contour), (2) at the bearing bracket and (3) at the stud bolt. The aim of this selection was to cover a broad and representative range of solidification conditions. At the specimen locations, between the liquidus and the solidus temperature, averaged cooling rates of approximately 0.1 to 8 K s^{-1} were measured.

The cylinder head casting, utilised for a four cylinder engine, was cast by Nematik Linz, Austria, using the Rotacast® process [29,30]. The Rotacast process offers excellent flexibility and is used to generate high quality castings. Through the use of active cooling applied to specific regions of the mold, local microstructural properties can be controlled and the process time can be reduced. Cores are shot in an external process, buffered and placed in the mold during each cycle of the process. The melt is automatically transferred from a holding furnace into a tundish. The tundish pivots under the closed mold and is pressed against it. Within the casting process a turning motion by 180° takes place which ensures a smooth filling and a natural solidification from the bottom (firedeck) to top (feeder). Three alloys were cast. The first alloy was Al-8Si-3Cu, which was grain refined and Sr modified. The second alloy was Al-7Si-0.5Cu-Mg with low amounts of Fe, which was grain refined and Sr modified. The third alloy was Al-7Si-0.5Cu-Mg with low amounts of Fe, which was grain refined and Na modified. The casting process for these alloys exhibits a wide range of solidification rates. At the specimen locations,

between the liquidus and the solidus temperature, averaged cooling rates of approximately 0.1 to 3.5 K s^{-1} were measured. Three areas of the casting were selected for removal of specimen material and analysis: (1) the fire deck, (2) the tween deck and (3) the camshaft bearing. The aim of the selection was to cover a broad range of solidification conditions. All three alloys were rotary degassed just before casting.

2.2. X-ray tomography and data generation

Sixty specimens were scanned with a GE nanotom m micro-XCT system at the Materials Center Leoben Forschungs GmbH, Leoben, Austria. The radiation source is a 10–180 kV nano focus X-ray tube with internal cooling and a diamond window target, which can provide a focal spot size as small as 800 nm. The detector is a DX500L ($300 \times 240 \text{ mm}$) with 3000×2400 pixels resolution, $1.5 \times \text{IMR}$ and 10,000:1 dynamic range. For each alloy and modification variant (Al-8Si-3Cu-(Sr), Al-7Si-0.5Cu-Mg-(Sr) and Al-7Si-0.5Cu-Mg-(Na)) five specimens per position (three positions per casting) were scanned. Voxel sizes of 3 and $8 \mu\text{m}$ were used, depending on the size of the anticipated microstructural fineness. The voxel size is the edge length in x , y , and z of a cube shaped voxel, the three-dimensional equivalent to a two-dimensional pixel. The scanned specimens were cylindrically shaped with a minimum diameter of 6 mm and a fillet radius of 25 or 60 mm. Two defined heights of the scanned volume, namely of 5.4 mm and 15.5 mm, were scanned with resolutions of 3 and $8 \mu\text{m}$, respectively. The scanned volumes are therefore approximately 144 and 477 mm^3 by the arithmetic mean of all scans.

The scanned data was analysed by determining whether a voxel corresponds to a pore volume or a volume of dense solid matrix material. This was done by a self-determined consistent threshold value on the upper border of an acceptable threshold range. Afterwards, the resolution of the resulting pore volumes was artificially increased by a digital super resolution imaging technique [31]. Adjacent pores were 'merged' and analysed as one bigger pore if the distance between two pores met or fell below the spherical diameter (see Equation (3)) of the smaller pore [32]. An example of a three-dimensional rendering of pores within an Al-8Si-3Cu-(Sr) alloy specimen from the crankcase casting is shown in Figure 1. The analysis routine was developed by the Lehrstuhl für allgemeinen Maschinenbau of Montanuniversität Leoben in Austria.

2.3. Data analysis

After the XCT data had been processed, data analysis was conducted and characteristic measures of the porosity were defined. These measures are defined as given below. The total pore volume V_p is given by

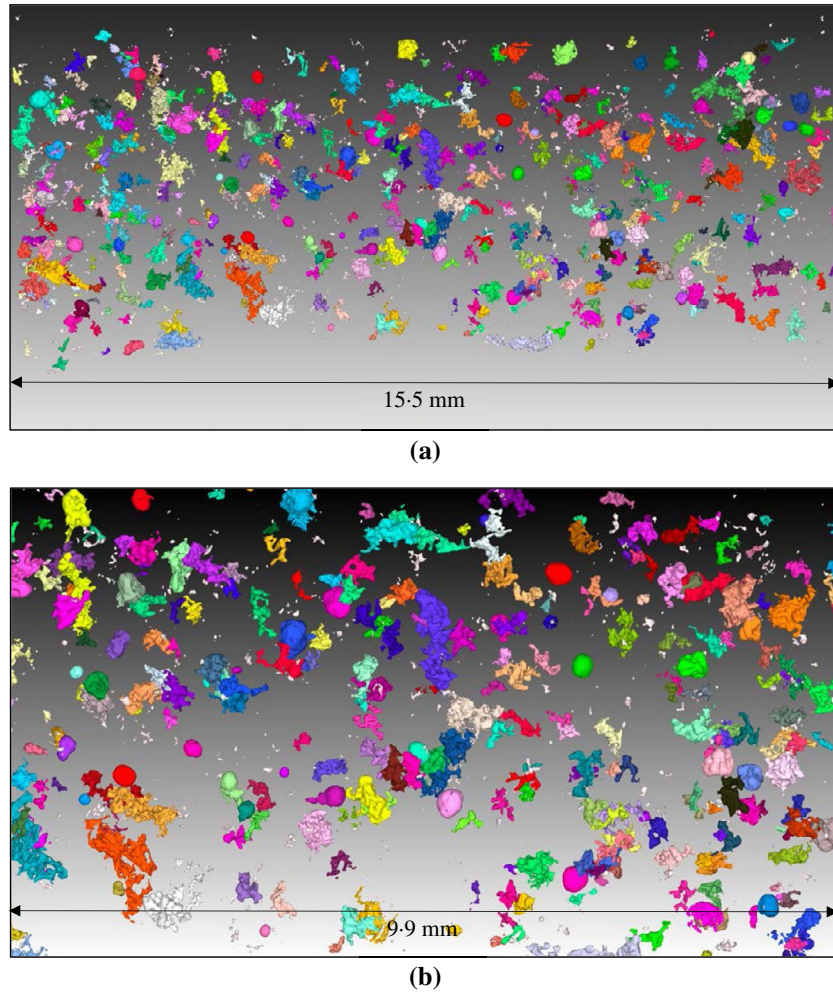


Figure 1. (a) Three-dimensional rendering of a full XCT scan (round bar specimen with a diameter of approximately 6 mm) and (b) a smaller region of interest of the same specimen extracted from an Al–8Si–3Cu–(Sr) cast crankcase stud. The specimen was scanned with 8 μm voxel size, and has a total porosity of $g_p = 0.58\%$, an SDAS of $\lambda_2 = 79 \mu\text{m}$ and a mean sphericity of $\phi_{\text{mean}} = 0.53$. Note that in the same sample there is a mixture of high and low sphericity pores.

$$V_p = \sum_N v_{p,i} \quad (1)$$

where N is the total number of pores in the scan and the volume of each pore is $v_{p,i}$ with $i = 1, 2, 3, \dots$. The volume averaged porosity (%) in the scan is therefore

$$g_p = \frac{V_p}{V_0} 100 \quad (2)$$

where V_0 is the total volume of the scan. Next, the spherical diameter $d_{s,i}$ of a pore is defined, which is the diameter of an equivalent spherical volume to the pore volume (as shown in Figure 2(a)), given by

$$d_{s,i} = \sqrt[3]{\frac{6v_{p,i}}{\pi}} \quad (3)$$

Subsequently the maximum spherical diameter $d_{s,max}$ is defined as the largest spherical diameter in a given specimen. To describe the maximum dimension of a

pore, the concept of a convex pore envelope is used. The pore envelope diameter $d_{e,i}$ as shown in Figure 2(b), is defined as the largest diameter of the convex envelope. Analogous to the maximum spherical diameter, a maximum envelope diameter $d_{e,max}$ is defined as the largest $d_{e,i}$ in a given specimen. To describe the mean pore and mean envelope sizes, a volume weighted mean is defined for both quantities. The mean spherical diameter is given by

$$d_{s,mean} = \frac{\sum_N (v_{p,i} d_{s,i})}{\sum_N v_{p,i}} \quad (4)$$

and the mean envelope diameter by

$$d_{e,mean} = \frac{\sum_N (v_{p,i} d_{e,i})}{\sum_N v_{p,i}} \quad (5)$$

where $d_{s,i}$ and $d_{e,i}$ are the spherical and envelope diameters for a given pore i for $i = 1, 2, 3, \dots$. The method and practice used to calculate a volume weighted mean, also

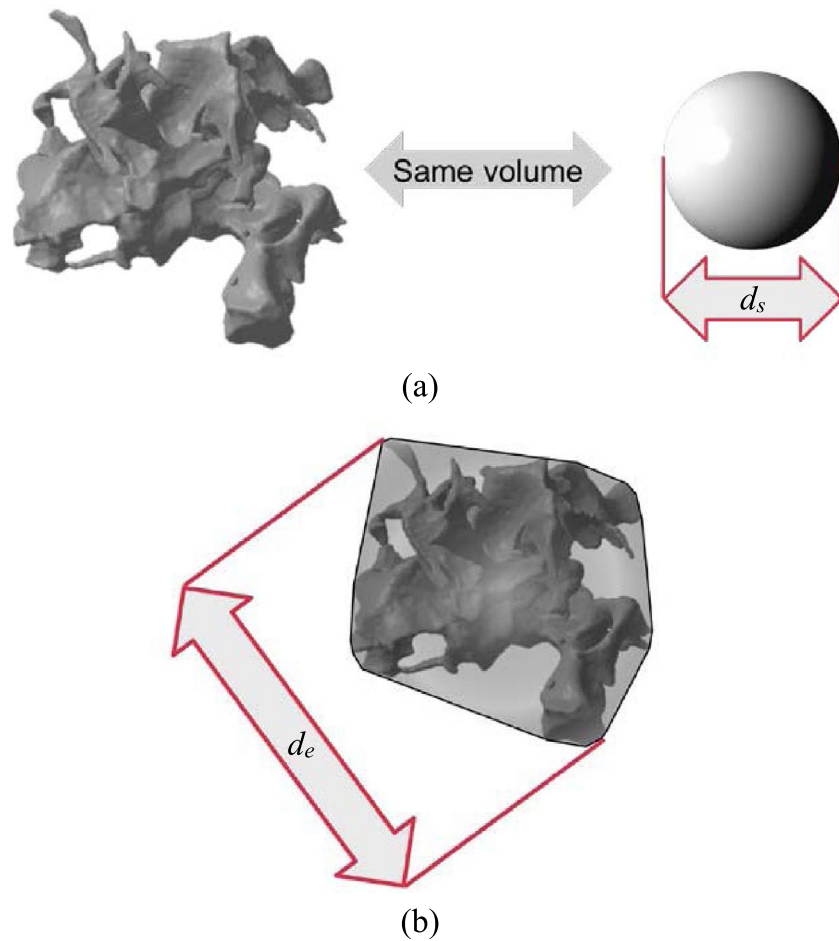


Figure 2. (a) A pore volume and an equivalent sphere having the same volume with diameter d_s and (b) the convex envelope diameter d_e .

called 'De Brouckere Mean', are described in the literature [33].

To characterise the morphological features of the porosity distributions, two additional quantities were introduced. One quantity is the sphericity ψ_i of a pore i as given by

$$\psi_i = \frac{\pi^{\frac{1}{3}} (6V_{p,i})^{\frac{2}{3}}}{s_i} \quad (6)$$

where s_i is the surface area of pore i , and the other quantity is the volume weighted mean sphericity ψ_{mean} given by

$$\psi_{mean} = \frac{\sum_N (v_{p,i} \psi_i)}{\sum_N v_{p,i}} \quad (7)$$

which from here on is referred to as the mean sphericity.

3. Results

Table 1 summarises important measured data and the defined characteristic quantities for the eight specimens that were selected for detailed analysis. Due to space limitations, these specimens are the basis for presenting

the characteristic developments in size, distribution, and morphology of the observed microporosity. The samples extracted from the production castings exhibit a broad range of secondary dendrite arm spacings (17 to 79 μm). Casting under automated industrial production line conditions ensures realistic, relevant and reproducible microstructures. The two alloys and two modifiers are often used in the casting industry. Also, the relatively low porosity amounts (see Table 1) found in slowly solidifying regions demonstrate the high quality manufacturing potential of the two processes applied here.

3.1. Porosity distribution

In Figure 3(a)–(h), the equivalent spherical pore size distributions of the eight selected specimens (already introduced in Table 1) are shown, plotted as the volume fraction of porosity g_p in respective diameter size bins. Specimen 1 (Figure 3(a)) displays a distribution of porosity with its maximum in the medium sized bins. A similar porosity distribution can be observed for specimens 3 (Figure 3(c)), 5 (Figure 3(e)), and 7 (Figure 3(g)). Specimen 3 has a relatively flat porosity distribution in the lower half of the bins and a few pores of much larger size. This kind of distribution is typical for cylinder head specimens

Table 1. List of selected CT specimens with key measurements and porosity data.

Specimen	Cast part	Position	Alloy	Modification	XCT voxel size/ μm	SDAS, $\lambda_2/\mu\text{m}$	Porosity, $g_p/\%$	Spherical Mean Diameter, $d_{s,mean}/\mu\text{m}$	Maximum Spherical Diameter, $d_{s,max}/\mu\text{m}$	Envelope Mean Diameter, $d_{e,mean}/\mu\text{m}$	Maximum Envelope Diameter, $d_{e,max}/\mu\text{m}$	Mean Sphericity, ϕ_{mean}
1	Cylinder head	Camshaft bearing	Al-7Si-0.5Cu-Mg	Sr	3	67	0.073	102	211	422	1242	0.43
2	Crank-case	Bridge	Al-8Si-3Cu	Sr	3	17	0.074	25	114	68	460	0.69
3	Cylinder head	Tween deck	Al-8Si-3Cu	Sr	8	54	0.176	251	518	1114	2753	0.31
4	Cylinder head	Fire deck	Al-7Si-0.5Cu-Mg	Na	3	30	0.181	124	222	288	596	0.57
5	Cylinder head	Camshaft bearing	Al-8Si-3Cu	Sr	8	58	0.358	398	728	1614	3961	0.22
6	Cylinder head	Tween deck	Al-7Si-0.5Cu-Mg	Na	8	56	0.379	253	362	452	1035	0.70
7	Crank-case	Stud bolt	Al-8Si-3Cu	Sr	8	78	0.813	299	577	818	2056	0.44
8	Cylinder head	Fire deck	Al-7Si-0.5Cu-Mg	Na	3	30	0.842	322	415	760	1341	0.54

of the Al-7Si-0.5Cu-Mg-(Sr) alloy above 0.03% porosity and for crankcase specimens of the Al-8Si-3Cu-(Sr) alloy above 0.3% porosity. Specimen 2 (Figure 3(b)) displays a porosity size distribution with its maximum in the lowest third of the bins. In the bin of $14 \mu\text{m} < d_s \leq 21 \mu\text{m}$ more than 25% of the total porosity of the specimen is measured. Cylinder head specimens from the Al-7Si-0.5Cu-Mg-(Sr) alloy with less than 0.03% porosity and crankcase specimens from the Al-8Si-3Cu-(Sr) alloy with less than 0.1% porosity show this kind of distribution. If the amount of porosity rises above 0.03% for the first or 0.3% for the latter alloy, the distribution shifts to a normal distribution as described above. Specimen 4 (Figure 3(d)) shows a bimodal distribution with two maxima, one in the lowest fourth and one in the upper third of the bins. The bin marking the lower maxima contains about 10%, and the bin marking the upper maxima contains about 20% of the total porosity. Of the sixty specimens, this type of distribution was found in only three specimens from the Al-7Si-0.5Cu-Mg-(Na) alloy cylinder head casting with approximately 0.2% averaged porosity. For specimens with less than approximately 0.1% porosity the majority of the pore volume is located in the medium or smallest pores. Specimens with more than approximately 0.3% porosity show a distribution with its maximum in the higher bins. So, the bimodal distribution may be a transition between specimens with very low and higher porosity levels. Specimens 6 (Figure 3(f)) and 8 (Figure 3(h)) show a size distribution of porosity fraction with its maximum in the upper third of the bins. Similar to specimen 2 (Figure 3(b)), the bin marking the maximum of the size distribution contains about 25% of the total porosity. This size distribution of pore volume is typical of those found in the cylinder head specimens from the Al-7Si-0.5Cu-Mg-(Na) alloy with more than 0.3% porosity. For the Al-8Si-3Cu-(Sr) alloy cylinder head specimens the behaviour is not as clear as for the other alloys. Up to approximately 0.26% porosity a distribution may have its maximum in the low bins or a normal distribution. Above 0.26% porosity the normal porosity distribution dominates.

Pores in the smallest third of bins represent a significant amount of the total porosity for specimens with a low overall porosity level ($g_p < 0.03\%$ for Al-7Si-0.5Cu-Mg-(Sr) cylinder head and a volume averaged porosity $g_p < 0.1\%$ for Al-8Si-3Cu-(Sr) crankcase). This distribution type is likely to correspond to a high density of pores nucleating in the final stages of solidification. The liquid areas (or pools) are hard to feed and the room for pore growth is strongly limited by the solid phase. So, although the pores are very small, they accommodate most of the porosity volume.

The bimodal distribution of the porosity fraction is an exception in the present study, since it is observed in only three of sixty specimens, and may be a transition distribution between very low (below 0.1%) and higher porosity amounts (above approximately 0.3%).

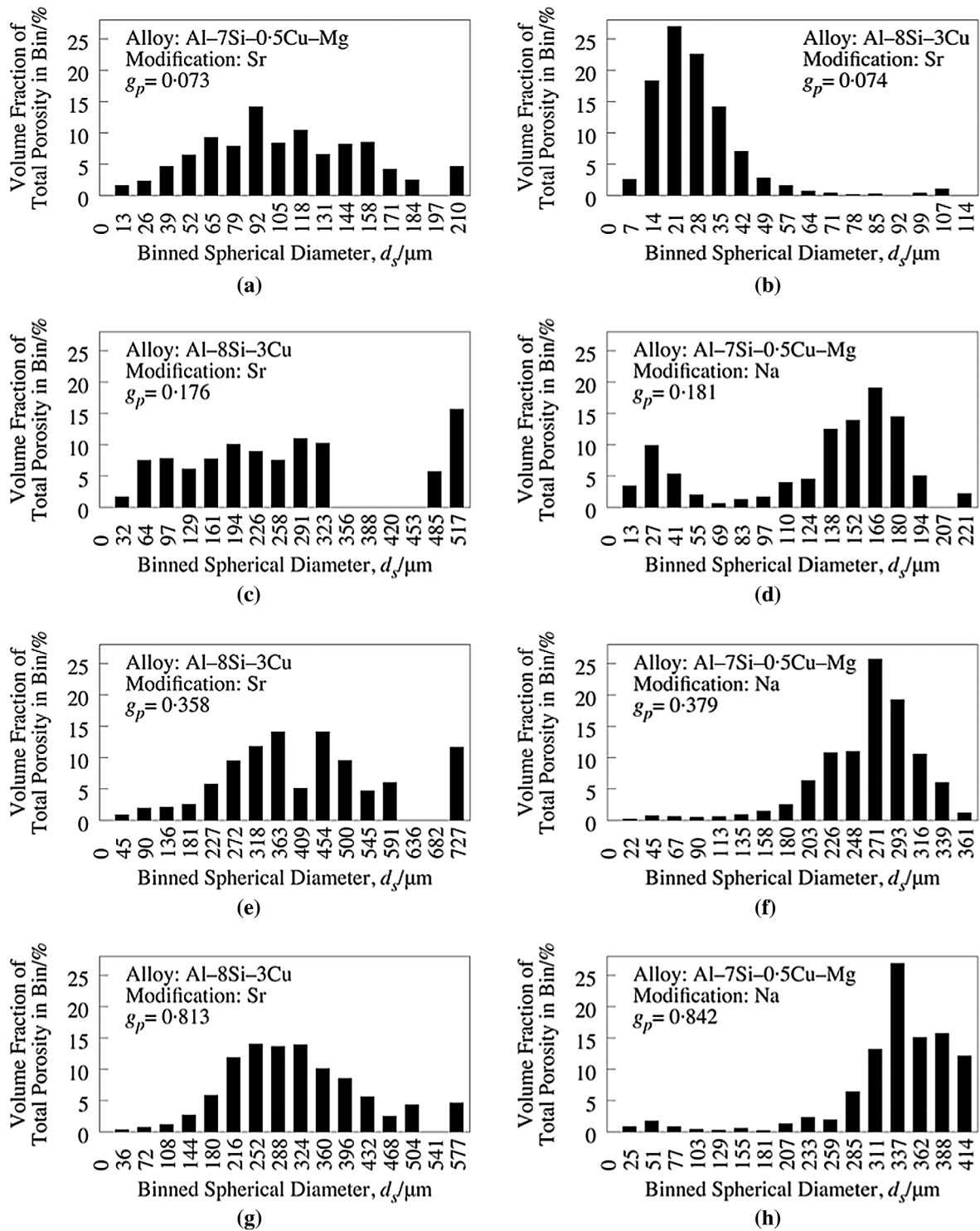


Figure 3. Histogram plots of pore size distribution showing volume fraction of total porosity in spherical diameter bins for specimens 1–8 in (a)–(h), respectively.

The occurrence of the bimodal size distribution might be explained by the mixture of dominant early stage pores and a high density of late stage porosity occurring at the spatial resolution limit. Although some of the solidification shrinkage is compensated by early pore formation, probably due to an increased gas content of the melt and sufficient time for hydrogen diffusion, the permeability drop in the mushy zone during the final solidification stage was high enough to produce a large number of isolated liquid pools.

It is conspicuous that a porosity distribution where most of the pore volume is represented by the larger and largest pores is almost exclusively represented by the Na modified specimens. If the majority of the porosity is located in the largest pores, these pores have to form early during solidification, grow for an extended period and compensate most of the volume deficit in the last stage of solidification. The morphological differences and possible explanations for these are discussed in greater detail in Section 3.4.

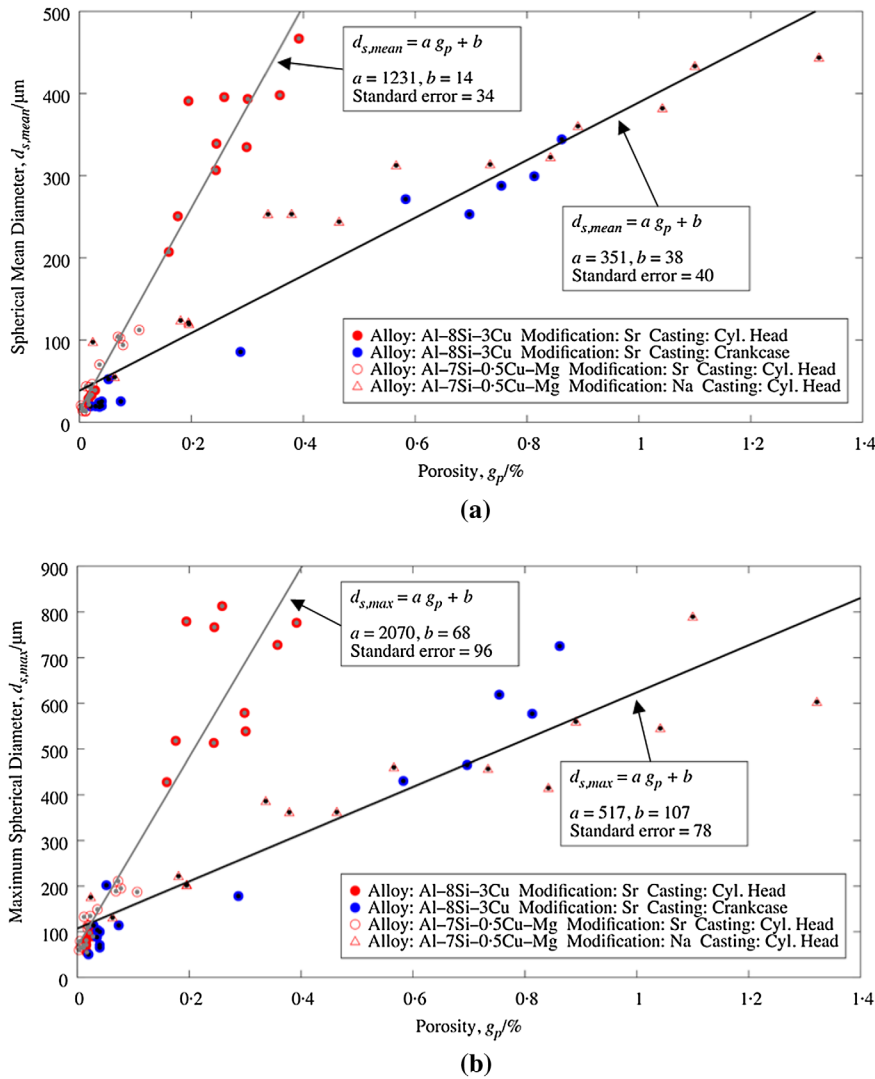


Figure 4. Plots of (a) the spherical mean diameter and (b) maximum spherical diameter vs. averaged porosity. Grey dots mark the specimens used for the 'grey' curve fit; black dots mark the specimens used in the 'black' fitted curve.

3.2. Correlations between spherical and envelope diameters and average porosity

Data and correlations between the volume averaged porosity and pore size measures as defined by the diameter of an equivalent sphere and the pore envelope diameter are given in Figures 4 and 5, respectively. For both size measures, the mean size determined by volume weighted averaging is given first (i.e. Figures 4(a) and 5(a)) and then the maximum of the size measure follows (i.e. Figures 4(b) and 5(b)). It was found that weighting the mean pore size measures by their volume removed the influence of the many small pores detected at the finer scan resolution in determining characteristic pore sizes. A simple arithmetic mean did not produce a reasonable analysis of the data measured with varying spatial resolutions. Not only could resolution differences in XCT scanning be compensated for by volume averaging, but the higher weighting of the largest pores in the averaging correctly reflects their relevance to fatigue performance. Note that the maximum pore size measures in Figures 4(b) and 5(b) are the diameter of the equivalent

sphere corresponding to the single pore with the highest volume, and the largest envelope diameter in the specimen, respectively.

For the entire data-set, the lowest and highest measured values of g_p range from 0.003 to 1.322%, respectively. For the sixty specimens measured using XCT and analysed to produce Figures 4 and 5, the relationship between the volume averaged porosity g_p and the mean and maximum pore size diameters show increasing diameters with increasing porosity, with two distinct trends in the data leading to an angled v-shaped boundary. The two trends are consistently followed in Figures 4 and 5 according to the four experimental datasets subdivided by alloy, modification, component cast and casting process. In all figures, the steeper leg of the v-shaped boundary is populated by data marked with grey dots. Referring to this as the grey population (GP), it is composed of the Al-8Si-3Cu-(Sr) cylinder head and Al-7Si-0.5Cu-Mg-(Sr) cylinder head data, with both cast in the Rotacast process. The second population in the figures has a trend showing a less steep pore size

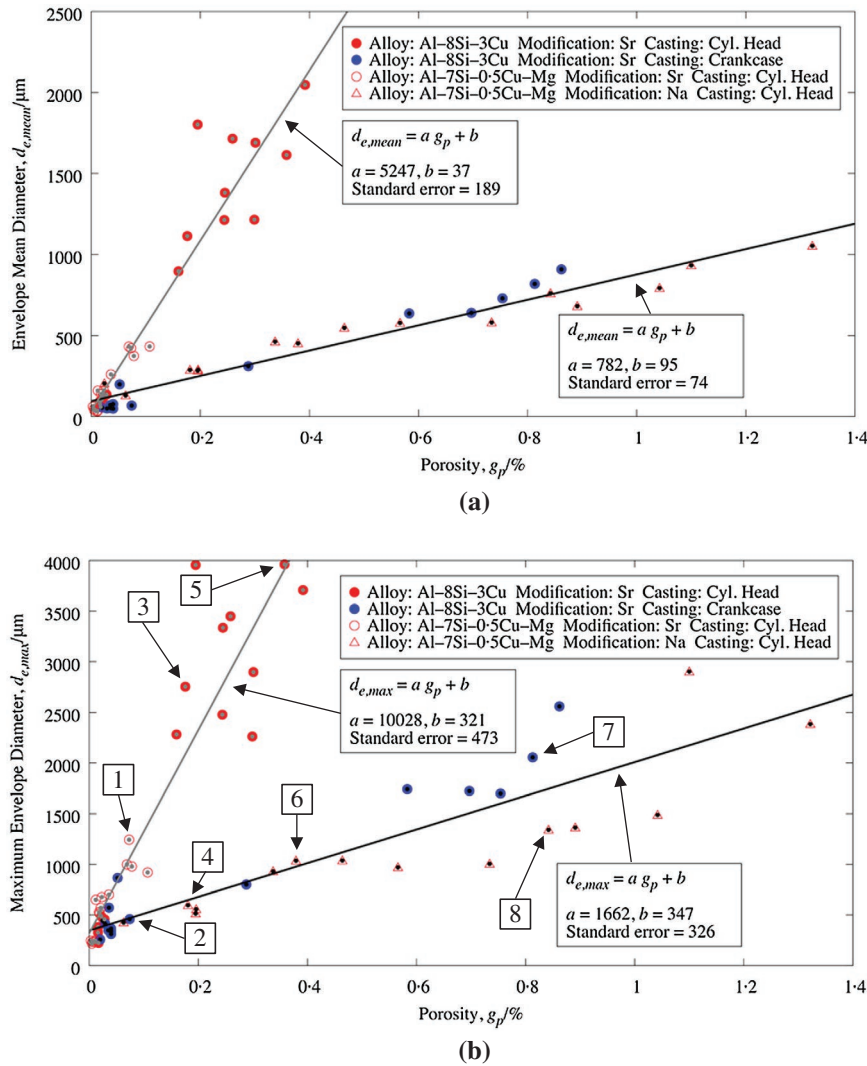


Figure 5. Plots of (a) the envelope mean diameter and (b) maximum envelope diameter vs. averaged porosity. Grey dots mark the specimens used in the grey fitted curve; black dotted specimens are taken into account for the black fitted curve. Note that the specimens labelled with 1 to 8 are shown later in Figures 7 and 8. Specimen pairs 1 and 2, 3 and 4, 5 and 6, and 7 and 8 were chosen for comparison in (b) based on their comparable porosity levels.

increase with g_p and is marked by black dots. Referring to this as the black population (BP), it is data from the Al-8Si-3Cu-(Sr) crankcase cast in the CPS process and the Al-7Si-0.5Cu-Mg-(Na) cylinder head cast in the Rotacast process. Comparing alloy composition, modification, casting process, and components cast for the two populations, no single casting condition clearly determines by itself the g_p -pore size relationship. There is an indication that modifier might determine the behaviour, since the cylinder head material cast by the Rotacast process from Al-7Si-0.5Cu-Mg-(Sr) to Al-7Si-0.5Cu-Mg-(Na) are in different populations. Slight differences in Si and larger differences in Cu content are apparent within the GP, but the modification, casting process and casting are the same. Those compositional differences do not alter the g_p -pore size relationship. Concluding general observations for Figures 4 and 5 for all porosity volume-size relationships, casting process and cast component are different for the data produced from the Al-8Si-3Cu-(Sr) material in the GP (cylinder head and Rotacast process) and BP (crankcase and CPS process),

which indicates casting process might play a role in the porosity volume-size relationship.

Linear correlations were generated for the GP and BP datasets corresponding to all 'legs' of the v-shaped boundaries in Figures 4 and 5. While the correlations are given in the figures, they are provided below in discussion of the individual figures. For the mean spherical pore diameter data plotted in Figure 4(a) the correlation for the steeper sloped GP data is

$$d_{s,mean} = 1231g_p + 14 \quad (8)$$

and for the BP it is given by

$$d_{s,mean} = 351g_p + 38 \quad (9)$$

In Figure 4(a), the minimum spherical mean diameter is 13 μm for all data. The maximum values of $d_{s,mean}$ of both specimen populations show little difference (GP: 467 μm ; BP: 444 μm), but maximum values are reached at significantly different porosity levels (GP: 0.392%; BP: 1.322%). The Al-8Si-3Cu-(Sr) specimens in the GP show porosity ranging from very low levels to the highest porosity

levels, and the Al–7Si–0.5Cu–Mg–(Sr) GP specimens have consistently low porosity levels, below 0.107%. Both BP alloys have porosity levels ranging from very low to the highest levels observed.

The maximum spherical diameter $d_{s,max}$ vs. porosity g_p plotted in Figure 4(b) are correlated for the GP by using

$$d_{s,max} = 2070g_p + 68 \quad (10)$$

and in case of the BP by using

$$d_{s,max} = 517g_p + 107 \quad (11)$$

The maximum spherical diameter in Figure 4(b) is not a weighted mean value. Approximately the same maximum spherical diameter is observed in both specimen populations (GP: 813 μm ; BP: 789 μm) but at significantly different levels of porosity (GP: 0.259%; BP: 1.1%). The lowest and highest values of $d_{s,max}$ of all specimens are 51 and 813 μm , respectively.

The envelope mean diameter $d_{e,mean}$ vs. the volume averaged porosity g_p is plotted in Figure 5(a). Again for the GP the size measure increases more rapidly with increasing porosity than for the BP, and is correlated by

$$d_{e,mean} = 5247g_p + 37 \quad (12)$$

In case of the BP the correlation is

$$d_{e,mean} = 782g_p + 95 \quad (13)$$

By definition, the values of the envelope mean diameter $d_{e,mean}$ are larger than the spherical mean diameter $d_{s,mean}$ in Figure 4(a). Unlike that figure, the largest envelope mean diameters for the GP and BP are now significantly different in Figure 5(a). The maximum values of the envelope mean diameter in Figure 5(a) are almost different by a factor two (GP: 2505 μm ; BP: 1426 μm). The minimum and maximum values of $d_{e,mean}$ are 87 and 2505 μm , respectively.

For the maximum envelope diameter $d_{e,max}$ vs. volume averaged porosity g_p data in Figure 5(b) the correlation for the GP having the steeper slope is

$$d_{e,max} = 10028g_p + 321 \quad (14)$$

and for the BP is

$$d_{e,max} = 1662g_p + 347 \quad (15)$$

Note the large defect sizes by this measure of pore diameter relative to the small amount of the associated porosity levels (about 4 mm at 0.2% porosity for the GP).

Additional insight into the pore size–volume relationships is gained by considering the eight specimens characterised by the data in Table 1 and identified by the numbered boxes in Figure 5(b). Three samples are from the GP (1, 3 and 5) and five specimens are from the BP (2, 4, 6, 7 and 8). These eight specimens are categorised within four porosity levels for direct comparison, roughly 0.1% for specimens 1 and 2, 0.2% for specimens 3 and 4, 0.4% for specimens 5 and 6, and 0.8% for specimens 7 and 8. Starting with the clearest difference

between the two populations by comparing specimens 5 and 6, specimen 5 has the largest maximum envelope diameter of all specimens and is a member of the GP ($d_{e,max}$ of GP: 3961 μm at 0.358% porosity). While Specimen 6 has a comparable level of porosity (0.379%) but has a maximum envelope diameter of 1035 μm (smaller by a factor of almost 4). Between specimens 1 and 2, and specimens 3 and 4, the differences in $d_{e,max}$ between populations have the same trend. Specimens 7 and 8 are both specimens of the BP, and the GP does not have porosity levels this high (about 0.8%). The maximum envelope diameters for specimens 7 and 8 have variability at a similar porosity level (Al–8Si–3Cu–(Sr): 2056 μm and Al–7Si–0.5Cu–Mg–(Na): 1341 μm . For all data there is increasing variability in $d_{e,max}$ with increasing porosity. The range of maximum envelope diameters observed for all specimens is from 218 to 3961 μm .

3.3. Maximum diameters versus mean diameters

Figure 6(a) shows the plot of the maximum spherical diameter $d_{s,max}$ vs. the spherical mean diameter $d_{s,mean}$. All sixty specimens are plotted and fitted by the linear function

$$d_{s,max} = 1.58d_{s,mean} + 45 \quad (16)$$

Clearly, there is a strong linear correlation, with the maximum spherical diameter being approximately 1.6 times larger than the mean. In contrast to the correlations presented in Section 3.2, there is no apparent distinction between characteristically different specimen populations here. The quality of the fit decreases slightly with increasing mean spherical diameter indicating that additional scatter and variability occur in distributions with larger pores.

Figure 6(b) shows the plot of the maximum envelope diameter $d_{e,max}$ vs. the envelope mean diameter $d_{e,mean}$. As in Figure 6(a) all sixty specimens are fitted by a linear function

$$d_{e,max} = 1.97d_{e,mean} + 213 \quad (17)$$

Again, the maximum envelope diameter is approximately two times larger than the mean and the quality of the fit decreases slightly with increasing mean envelope diameter.

It is shown in Figure 6 that both the maximum spherical diameter and the maximum envelope diameter correlate linearly with their respective mean values. This observation holds true for all sixty scans regardless of belonging to the two identified specimen populations. This finding is a key statement because the maximum pore size and its derived quantities are the most useful porosity measures in determining the effect of porosity on the fatigue of cast components [2,3]. If one can predict the means, the maxima can be obtained too. Considering the range of variation in the modification,

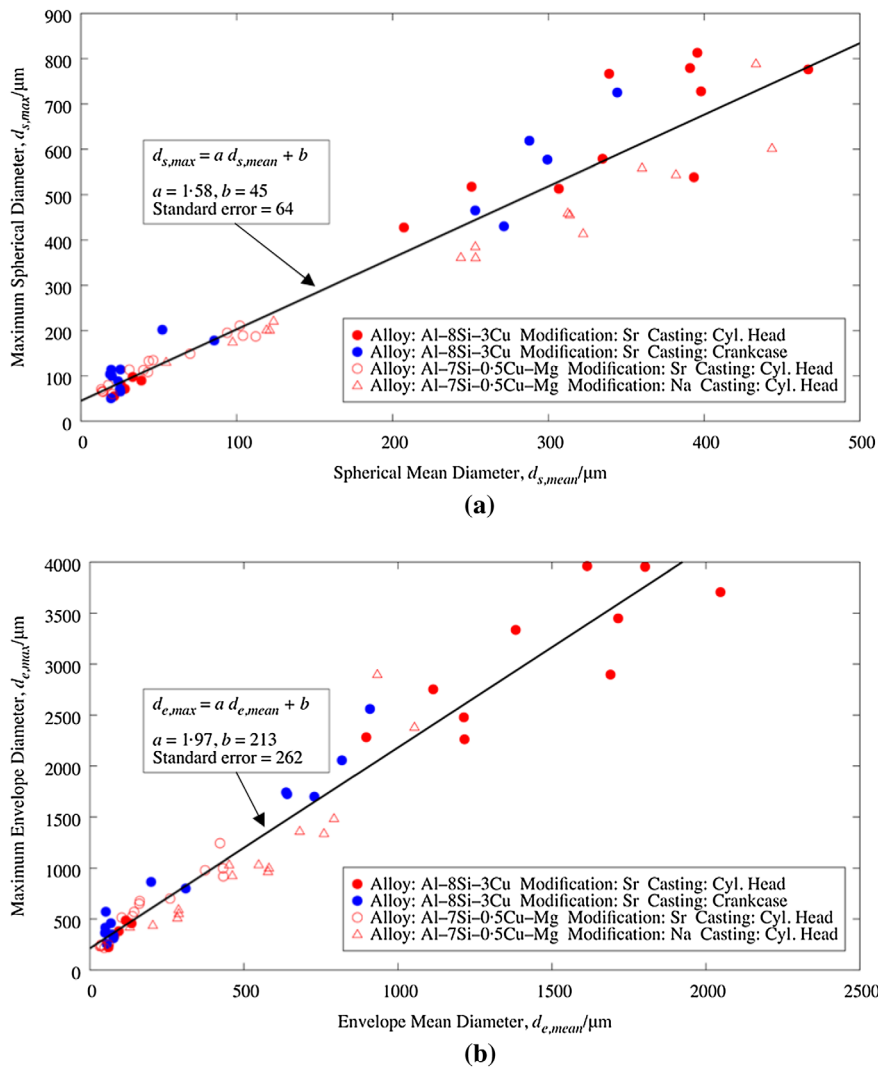


Figure 6. (a) Plots of the maximum spherical diameter vs. the spherical mean diameter and (b) the maximum envelope diameter vs. the envelope mean diameter.

All data points are taken into account for the linear fitted curves.

alloy composition and process method, the results in Figure 6 are surprisingly good.

3.4. Morphological observations about microporosity

Figure 7 shows the three-dimensional representation of the pores from the specimens 1, 2, 4 and 8; all scanned with a voxel size of 3 μm . Figure 8 depicts the segmented pores of specimens 3 and 5 and Figure 9 shows specimens 6 and 7; all scanned with a voxel size of 8 μm . Each identified pore is depicted in a randomly assigned colour for better visual interpretation. As stated before, specimen pairs 1 and 2, 3 and 4, 5 and 6, and 7 and 8 were selected for their comparable levels of porosity. Despite their similar porosity levels, each specimen pair at all four levels show clear differences in their pore morphology and distribution.

Specimen 1 (Figure 7(a)) shows, even at a very low porosity level of 0.073%, a tortuous pore morphology

with a large maximum envelope diameter of 1242 μm (see Table 1). Because of the pores' high tortuosity and larger surface area, the visual impression is that of a higher porosity level. In contrast, specimen 2 (Figure 7(b)) has a fundamentally different appearance in its pore volume distribution despite similar porosity volume. In specimen 2, the pores are in general smaller and not as tortuous as in specimen 1. Also for specimen 2, note that almost 50% of the porosity is distributed in very fine pores up to 21 μm spherical diameter.

Specimen 3 (in Figure 8(a)) has a higher porosity level of 0.176% than specimen 1, but a similar appearance with very tortuous pores with a large relative surface area. The pores' surfaces appear to follow along the dendritic microstructure of the primary aluminium phase. Specimen 4 (Figure 7(c)) has a porosity level of 0.181%, essentially the same as specimen 3. The pores in specimen 4 as visualised by the CT are not tortuous, but rather more round and spherical. Between the bigger pores in specimen 4 there are many evenly distributed tiny pores

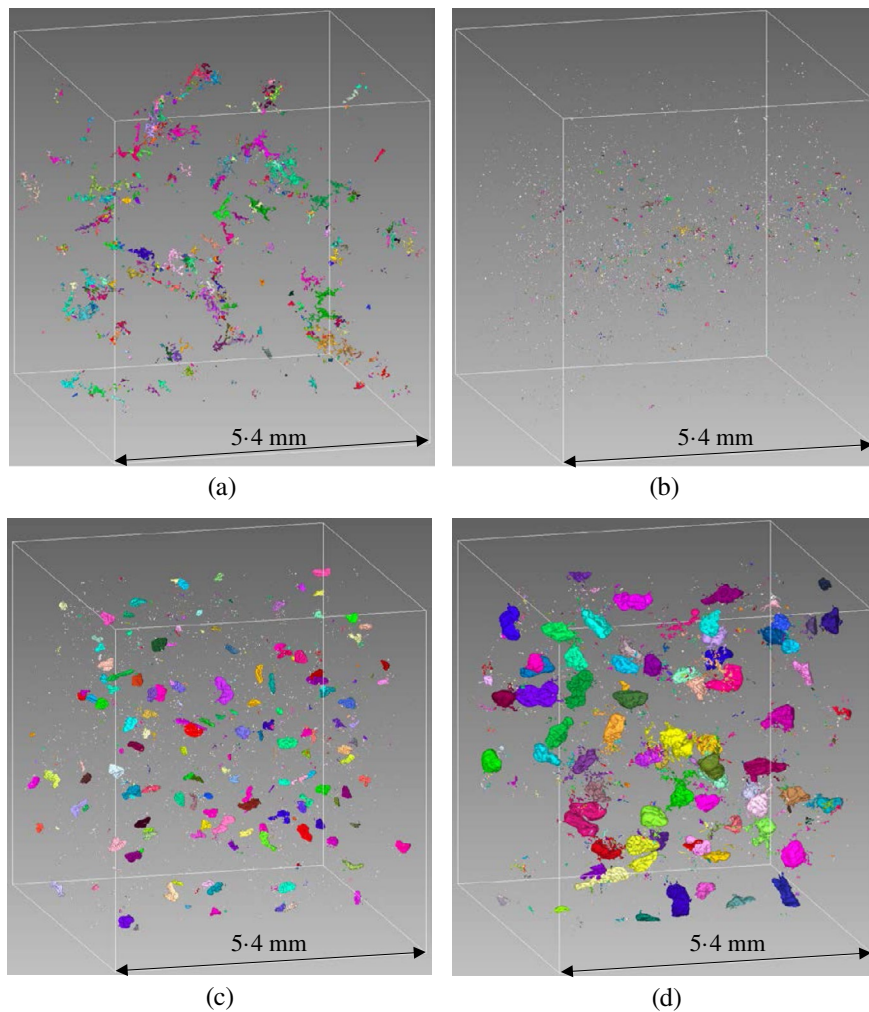


Figure 7. Pictures of selected XCT scans performed with $3\ \mu\text{m}$ voxel size with an approximate ROI of $144\ \text{mm}^3$: (a) Specimen 1, from Cylinder Head, Camshaft Bearing, Al-7Si-0.5Cu-Mg-(Sr), $\lambda_2 = 67\ \mu\text{m}$, $g_p = 0.073\%$, $\varphi_{\text{mean}} = 0.43$, $d_{e,\text{max}} = 1242\ \mu\text{m}$; (b) Specimen 2, from Crank Case, Bridge, Al-8Si-3Cu-(Sr), $\lambda_2 = 17\ \mu\text{m}$, $g_p = 0.074\%$, $\varphi_{\text{mean}} = 0.69$, $d_{e,\text{max}} = 460\ \mu\text{m}$; (c) Specimen 4, from Cylinder Head, Firedeck, Al-7Si-0.5Cu-Mg-(Na), $\lambda_2 = 30\ \mu\text{m}$, $g_p = 0.181\%$, $\varphi_{\text{mean}} = 0.57$, $d_{e,\text{max}} = 596\ \mu\text{m}$; (d) Specimen 8, from Cylinder Head, Fire Deck, Al-7Si-0.5Cu-Mg-(Na), $\lambda_2 = 30\ \mu\text{m}$, $g_p = 0.842\%$, $\varphi_{\text{mean}} = 0.54$, $d_{e,\text{max}} = 1341\ \mu\text{m}$. All four samples are indicated in Figure 5(b). Note the different appearance of the pore sizes and shapes especially for (a) with its low sphericity type of microporosity, whereas (c) and (d) show primarily high sphericity pores.

at the XCT resolution limit. These tiny pores make up the lower bins of the bimodal distribution in Figure 3(d) with a peak diameter at $27\ \mu\text{m}$ for specimen 4. Despite having the same porosity volume, specimen 3 has a $d_{e,\text{max}}$ of $2753\ \mu\text{m}$ and specimen 4 a $d_{e,\text{max}}$ of $596\ \mu\text{m}$ due to morphology differences (see Table 1).

The appearance of the porosity distribution and morphology visualised in specimen 5 (Figure 8(b)) is similar to that for specimen 3 (Figure 8(a)). Likewise the porosity features in specimen 6 (Figure 9(a)) are comparable to the features visualised in specimen 4 (Figure 7(c)). Because of the higher porosity volume in specimens 5 and 6 (approximately 0.36%), the tortuous shaped pores in specimen 5 and more spherical pores in specimen 6 are simply larger those in specimens 3 and 4, respectively. It is noteworthy that both specimens have roughly the same secondary dendrite arm spacing (SDAS) of $\lambda_2 = 57\ \mu\text{m}$ (compare Table 1).

So far, all visualisations of porosity distributions in the specimens have been from samples from the GP (1, 3 and 5) or the BP (2, 4 and 6). Distributions from BP specimens having the highest porosity level (of approximately 0.83%) are visualised for specimens 7 (Figure 9(b)) and 8 (Figure 7(d)). Noteworthy differences in the characteristic measures between these specimens show that Specimen 8 has a pore morphology similar to specimens 4 and 6, but the pores are larger, especially relative to the microstructural features ($\lambda_2 = 30\ \mu\text{m}$). Also, some pore surfaces show the complementary surface structure of the dendritic microstructure of the primary phase. The appearance of the porosity distribution in specimen 7 has some very distinct features which are typical of the observed pore morphology of only one experimental set, the Al-8Si-3Cu-(Sr) crankcase. It has tortuous pores comparable to the porosity of specimens 1, 3 and 5, but they are slightly more voluminous (inflated). In addition

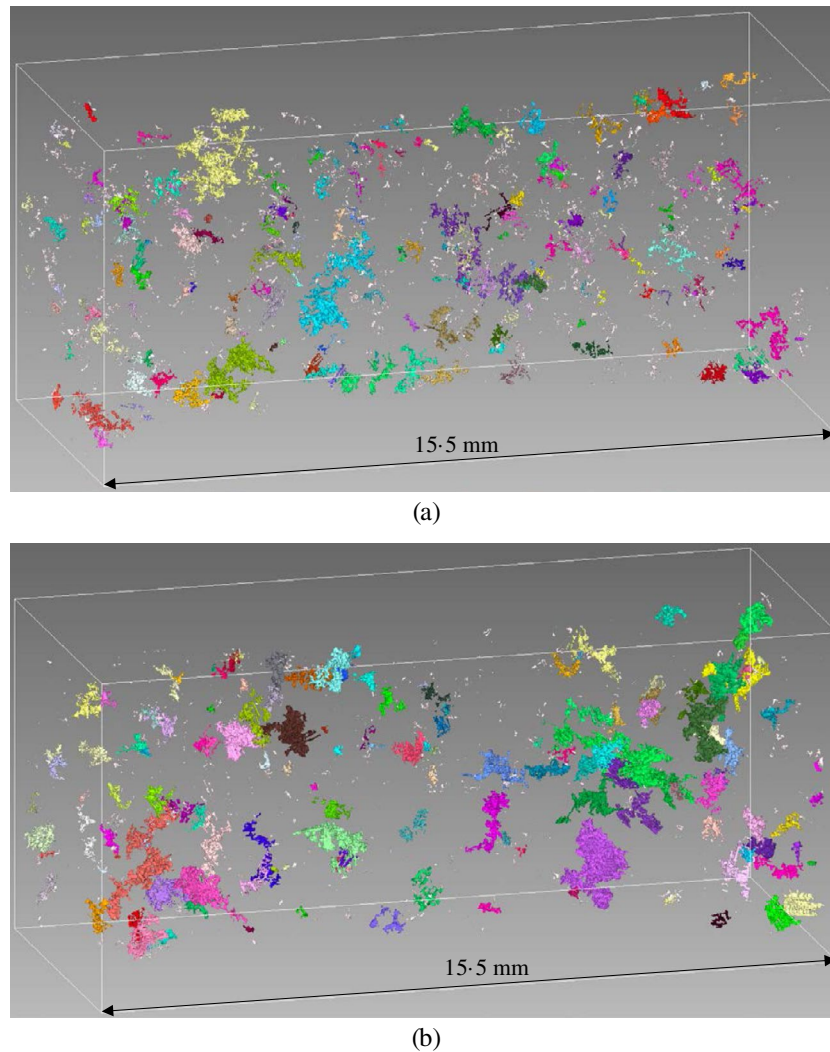


Figure 8. Pictures of representative XCT scans performed with $8\ \mu\text{m}$ voxel size with an approximate ROI of $477\ \text{mm}^3$: (a) Specimen 3, from Cylinder Head, Middle Deck, Al-8Si-3Cu-(Sr), $\lambda_2 = 54\ \mu\text{m}$, $g_p = 0.176\%$, $\varphi_{\text{mean}} = 0.31$, $d_{e,\text{max}} = 2753\ \mu\text{m}$; (b) Specimen 5, from Cylinder Head, Camshaft bearing, Al-8Si-3Cu-(Sr), $\lambda_2 = 58\ \mu\text{m}$, $g_p = 0.358\%$, $\varphi_{\text{mean}} = 0.22$, $d_{e,\text{max}} = 3961\ \mu\text{m}$; Both samples are indicated in Figure 5(b).

Note the low sphericity pores in (a) and (b), which results in high values of the maximum envelope diameter at relatively low porosity values.

to these tortuous pores, there are small to medium sized pores with a high (visual) sphericity present in specimen 7. While the larger tortuous pore surfaces show the microstructural dendritic features, the smaller spherical pores in specimen 7 do not. Specimen 7 shows both characteristic features of tortuous and spherical porosity. In Figure 1(b) another example of a porosity distribution with this dual character is also shown. It was found that specimens with porosity volumes less than 0.288% do not exhibit this dual morphology. It is noteworthy that none of the specimens showed a noticeable preferential direction regarding pore shape or morphology, and no anisotropy was found in the local pore density. All key measurements and porosity data are summarised in Table 1.

The discussion above and analysis of the pore morphologies explains the differences between the GP and BP. Specimens 4 (Figure 7(c)), 6 (Figure 9(a)) and 8 (Figure 7(d))

show porosity distributions forming at an early stage of solidification and represent the behaviour of the sodium modified experimental set. The pores must have formed early in solidification, probably due to the influence of hydrogen precipitation. They are not limited in growth by the dendritic network. Only for higher amounts of porosity (e.g. specimen 8) does impingement take place, making the dendritic structure visible on the pore surfaces. Hydrogen pick-up due to Na modification is described in the literature [34], and has been observed in experiments [35]. Na additions can modify the structure of the aluminium oxide layer and deteriorate its impermeability. This causes an increased hydrogen pick-up from the atmosphere. It is also likely that the mixture of tortuous and spherical pores in the Al-8Si-3Cu crankcase data (e.g. Figures 1 and 9(b)) is related to an increased hydrogen content. Though as noted here, a minimum porosity level (in this work more than 0.288%) has to

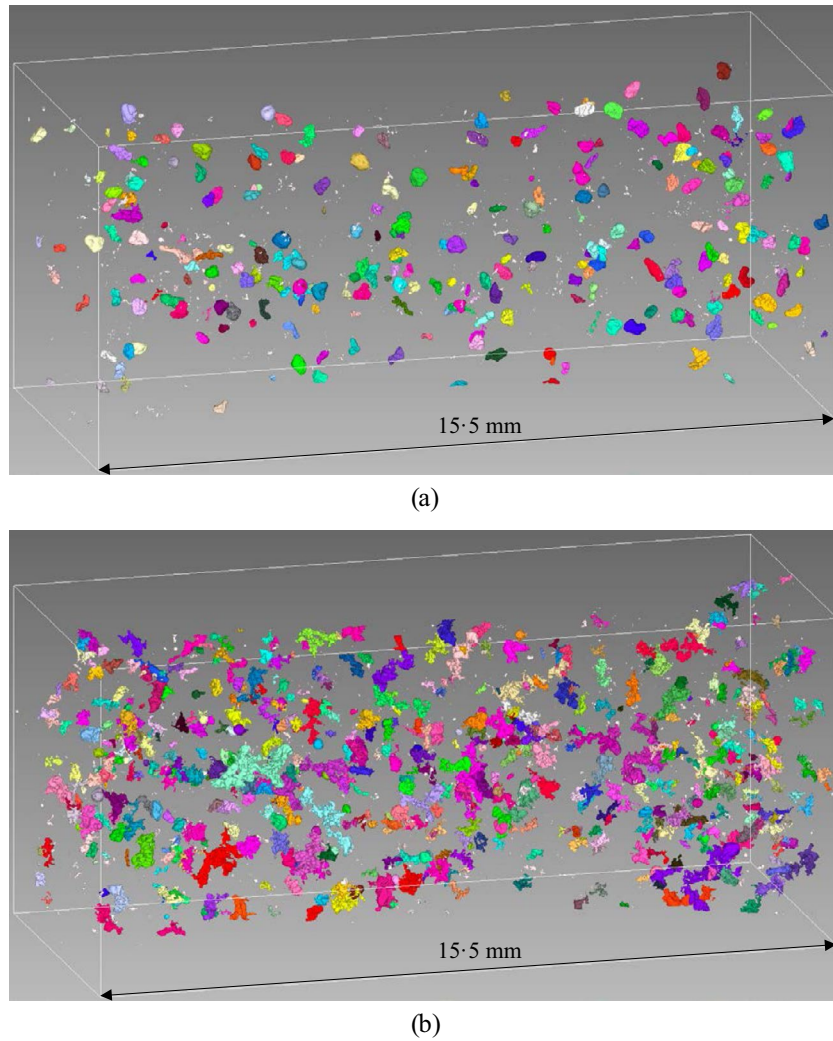


Figure 9. Pictures of selected XCT scans performed with 8 μm voxel size an approximate ROI of 477 mm^3 : (a) Specimen 6, from Cylinder Head, Middle Deck, Al–7Si–0.5Cu–Mg–(Na), $\lambda_2 = 56 \mu\text{m}$, $g_p = 0.379\%$, $\varphi_{\text{mean}} = 0.58$, $d_{e,\text{max}} = 1037 \mu\text{m}$; (b) Specimen 7, from Crank Case, Stud, Al–8Si–3Cu–(Sr), $\lambda_2 = 78 \mu\text{m}$, $g_p = 0.813\%$, $\varphi_{\text{mean}} = 0.44$, $d_{e,\text{max}} = 2056 \mu\text{m}$. Both samples are called out in Figure 5(b). Note the appearance of the high sphericity pores in (a) which lead to a relatively small maximum envelope diameter for the volume of porosity present. Specimen (b) contains a mixture of low and high sphericity pores.

be reached to observe this dual porosity morphology distribution. Unfortunately, this hypothesis cannot be proven here because of the lack of quantitative hydrogen measurements. The rotary degassed, and Sr modified experimental data from the Al–8Si–3Cu–(Sr) cylinder head and the Al–7Si–0.5Cu–Mg–(Sr) cylinder head show only very tortuous porosity. This can be associated with pore formation later during solidification and a low hydrogen content [36–39]. The pores have little room to form within the well advanced solidified network and are forced to adapt to a tortuous shape.

3.5. Sphericity

To quantify the pore morphological differences described in section 3.4, a mean sphericity ψ_{mean} was calculated for all specimens as given in Figure 10 plotted vs. porosity g_p along with two correlations. Pores for which no surface area could be calculated, or with a calculated sphericity above unity were excluded from the analysis. This was

found to occur primarily for pores close to the resolution limit because uncertainties in the volume and surface determination can lead to such unreasonable results.

As observed from Figures 5 and 6, the four sets of experimental data are divided into the same two characteristic pore populations (GP and BP) and are marked by grey and black dots, respectively. The correlation curves fitting the two populations in Figure 10 have three parameters (a, b, and c) and are given by

$$\psi_{\text{mean}} = \frac{a}{1 - be^{cg_p}} = \frac{0.08}{1 - 0.9e^{-1.09g_p}} \quad (18)$$

for the GP and

$$\psi_{\text{mean}} = \frac{a}{1 - be^{cg_p}} = \frac{0.56}{1 - 0.59e^{-29.94g_p}} \quad (19)$$

for the BP.

In Figure 10, the black curve fits the development of sphericity of the Al–8Si–3Cu–(Sr) crankcase and Al–7Si–0.5Cu–Mg–(Na) cylinder head experimental sets.

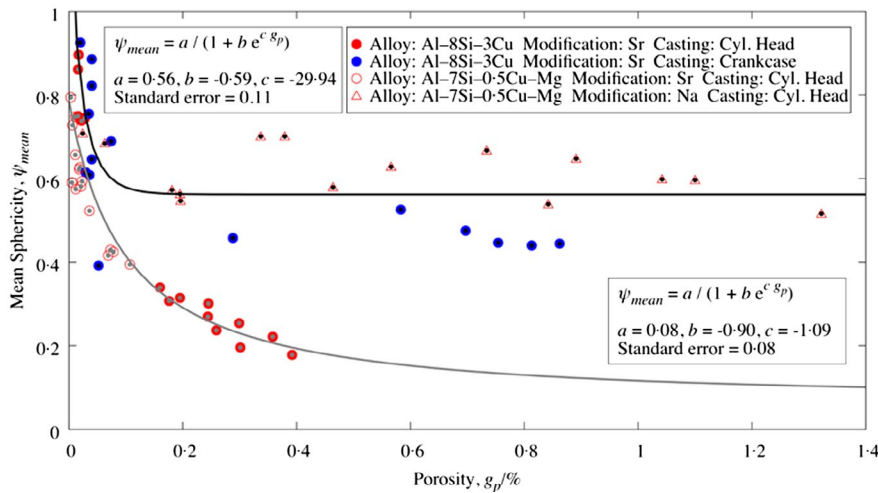


Figure 10. Plot of the mean sphericity vs. the averaged porosity.

Grey dots mark the points considered in the grey population correlation; black dots are used in the black population correlation. The sphericity of the black marked specimens approaches 0.56 at higher porosity values. The sphericity of the grey marked specimen behaves differently and approaches a lower value of 0.08 as porosity increases.

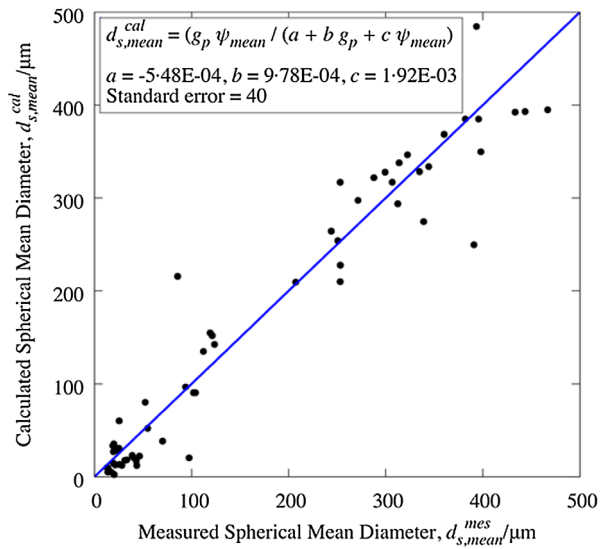
Specimens 2, 4, 6, 7 and 8 are members of the population where sphericity and porosity are described by this function. At 0.01% porosity this function reaches approximately 1, the limiting value. Above the porosity level of roughly 0.2%, the sphericity is constant at 0.56.

The grey curve fits the Al-8Si-3Cu-(Sr) cylinder head and Al-7Si-0.5Cu-Mg-(Sr) cylinder head experimental sets, and specimens 1, 3 and 5 are in this population. As the porosity approaches 0 for this curve, the mean sphericity goes to a limit of approximately 0.8. For the GP curve in Figure 10, the maximum porosity level of the data is about 0.4% where the sphericity drops to approximately 0.2. For higher porosity levels there is no data, and the extrapolated sphericity decreases to a limit of 0.08.

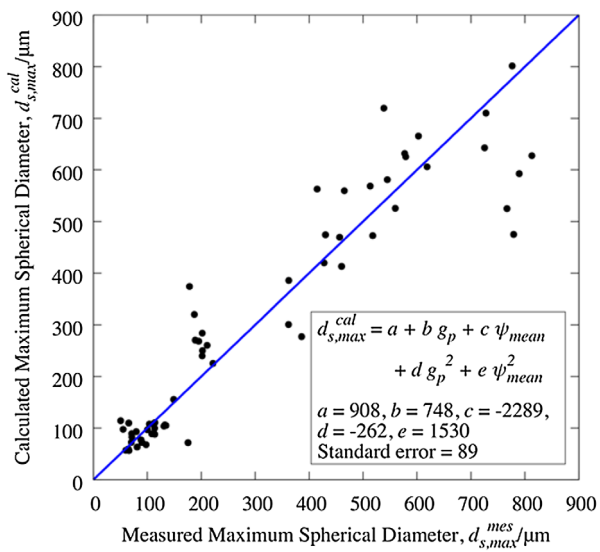
The sphericity of the GP and BP both show high mean sphericity values for very low porosity levels. The BP maintains a relatively high sphericity level even at higher porosity levels, which indicates that even the larger pores are closer to a spherical shape (see Figures 7(c) and (d) and 9(a)). The specimens from the Al-8Si-3Cu-(Sr) crankcase experimental data-set lie slightly under the GP curve fit, indicating that the mean sphericity for this data-set runs towards a slightly lower mean sphericity value. This observation is consistent with the mixture of tortuous and spherical pores (see Figures 1 and 9(b)) within the specimens. For the GP data, the sphericity drops continuously with increasing porosity, meaning that the pores' surface areas consistently increase relative to their volumes when compared to a sphere. The range of ψ_{mean} observed in the present work is from 0.18 to 0.93 (see Table 1 for a summary of the mean sphericity values of the eight representative specimens).

The observed pore morphologies are well represented by the mean sphericity given in Table 1 and plotted in Figure 10. In specimens with little porosity, the pores are small enough to fit into the interdendritic spaces partly confined by eutectic phase. Hence, the

presented high sphericity values for very low porosities are reasonable. As shown by Felberbaum et al. [27], pores in contact with the eutectic phase show a dominance of positive mean curvatures to satisfy the Laplace-Young equation, which is in agreement with the presented finding for low porosity specimens. With increasing amount of porosity, the sphericity decreases for both populations. The trend can be explained by pores having increasing interaction with the solid dendritic structure as porosity increases. Shrinkage driven pores are only able to increase their volume by increasing their tortuosity as they grow further into the solid mush. Because hydrogen driven, or generated, pores nucleate earlier, this effect is limited within the BP. Pores that nucleate early in solidification may even be able to push equiaxed crystals away, and increase their available space for further growth. This way the large pores found in specimens of the BP (e.g. specimen 8 (Figure 7(d)) adapt only slightly to the surrounding solid structure. This results in the correlation describing the BP to have a constant mean sphericity value of 0.56 above approximately 0.2% porosity (compare Table 1). The observed behaviour for the BP correlation is supported by Puncreobutr et al.'s [11] *in situ* observation of the growth of an individual pore. They measured a constant sphericity of approximately 0.6 above a pore volume of 0.025 mm³ (up to app. 0.054 mm³), which corresponds to a spherical diameter of $d_s = 363 \mu\text{m}$ ($d_s = 469 \mu\text{m}$). This value is representative for a medium sized high sphericity pore in the present assembled XCT data, and comes very close to the above mentioned constant mean sphericity value of 0.56 for the BP. Most likely for the BP, the amount of hydrogen introduced into the melt by the process (CPS), or by modification (Na), dominates the overall porosity morphology. On the other hand, the general level of local porosity in a casting may change significantly with composition, modification, Fe level or cooling rate.



(a)

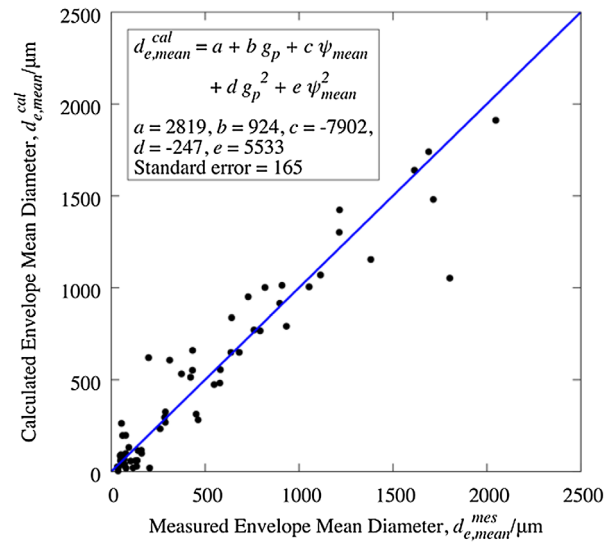


(b)

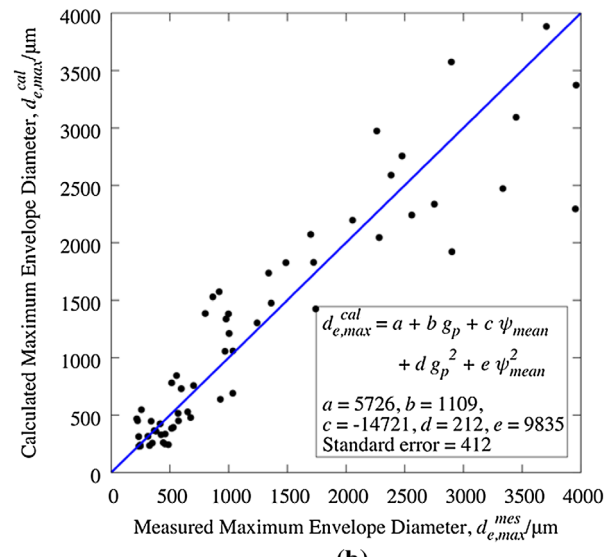
Figure 11. Plots of (a) the calculated spherical mean diameter vs. the measured spherical mean diameter and (b) the calculated maximum spherical diameter vs. the measured maximum spherical diameter.

3.6. Calculated versus measured characteristic quantities

It was demonstrated in Sections 3.2 and 3.3 that the four characteristic quantities ($d_{s,mean}$, $d_{s,max}$, $d_{e,mean}$ and $d_{e,max}$) show a good correlation with the averaged porosity g_p for both the GP and BP. Based on the findings presented in Sections 3.4 and 3.5, there is a fundamental difference between both identified pore populations with respect to their pore morphology. The goal of this section is to demonstrate the accuracy of the calculated characteristic quantities from the total amount of porosity g_p and the mean sphericity ψ_{mean} . If in fact the characteristic measures of the GP and BP can be accurately calculated from g_p and ψ_{mean} , there is strong evidence that the mean sphericity is the key quantity needed to describe the porosity characteristics. Functions incorporating these two parameters



(a)



(b)

Figure 12. Plots of (a) the calculated envelope mean diameter vs. the measured envelope mean diameter and (b) the calculated maximum envelope diameter vs. the measured maximum envelope diameter.

were developed and are noted in Figures 11 and 12. In these figures, the blue diagonal line indicates ideal agreement between calculation and measurement. The standard error is given in all four plots as an estimate of the quality of the fit between prediction and measurement.

Figure 11(a) shows the plot of the calculated spherical mean diameter $d_{s,mean}^{cal}$ vs. the measured spherical mean diameter $d_{s,mean}^{mes}$ as calculated by

$$d_{s,mean}^{cal} = \frac{g_p \psi_{mean}}{-5.48 \times 10^{-4} + 9.78 \times 10^{-4} g_p + 1.92 \times 10^{-3} \psi_{mean}} \quad (20)$$

Measurement and calculation correlate well. So, the spherical mean diameter is correlated not only with the porosity level (as already shown in Figure 4(a)), but also with the pore morphology described by the mean sphericity. By incorporating the mean sphericity of each

specimen, it is possible to collapse both population trend lines of Figure 4(a) into a single calculation.

Similarly, in Figure 11(b) the plot of the calculated maximum spherical diameter $d_{s,max}^{cal}$ vs. the measured maximum spherical diameter $d_{s,max}^{mes}$ is given. A good prediction of the maximum spherical diameter is given by

$$d_{s,max}^{cal} = 908 + 748g_p - 2289\psi_{mean} - 262g_p^2 + 1530\psi_{mean}^2 \quad (21)$$

Again, the correlation between prediction and measurement is good, and the differing behaviours of the GP and BP in Figure 4(b) can be explained by the pore morphological differences. The scatter between prediction and measurement increases slightly with higher values of the maximum spherical diameter.

In Figure 12(a) a plot of the calculated envelope mean diameter $d_{e,mean}^{cal}$ vs. the measured envelope mean diameter $d_{e,mean}^{mes}$ is shown. The equation applied for this calculation is

$$d_{e,mean}^{cal} = 2819 + 924g_p - 7902\psi_{mean} - 247g_p^2 + 5533\psi_{mean}^2 \quad (22)$$

Once more, the displayed correlation quality is good, and, analogous to the explanations above, the pore morphology is the key phenomena responsible for the two population trend lines of Figure 5(a).

Lastly, Figure 12(b) displays the plot of the calculated maximum envelope diameter $d_{e,max}^{cal}$ vs. the measured maximum envelope diameter $d_{e,max}^{mes}$. The maximum envelope diameter is calculated by

$$d_{e,max}^{cal} = 5726 + 1109g_p - 14721\psi_{mean} + 212g_p^2 + 9835\psi_{mean}^2 \quad (23)$$

Again, a good correlation between prediction and measurement is evident. Figure 5(b), showing two distinguishable population based correlations between porosity and the maximum envelope diameter that are now well described by a single calculation using the two parameters g_p and ψ_{mean} .

For the alloy systems examined and their casting conditions, if the amount of porosity and the mean sphericity is locally known (by measurement or prediction), measures describing the pore distribution ($d_{s,mean}$ and $d_{e,mean}$) and the maximum pore defect size ($d_{s,max}$ and $d_{e,max}$) can be calculated with reasonable accuracy. Still missing from this framework is a thorough understanding, or even a correlation, between the mean sphericity and the gas level of the melt. It might be possible to predict ψ_{mean} by g_p and the gas concentration, but to establish this correlation more research in this direction is needed.

It is shown that the characteristic measures $d_{s,mean}$, $d_{s,max}$, $d_{e,mean}$ and $d_{e,max}$ can be calculated with good accuracy by knowing the porosity g_p and mean sphericity ψ_{mean} . This finding supports the hypothesis that the local porosity size distribution (in the examined alloys

and process ranges) is sufficiently characterised by these two values, and they enable prediction of the pore size characteristics. Maximum defect size is the primary defect parameter that can be used in fatigue life prediction [4–9], and here a straight forward correlation (under the assumption that the porosity morphology is known) is established to calculate it. From the amount of porosity and knowledge of pore morphology, a significant relationship between cast material containing microporosity and its performance in service is developed, which will increase the capabilities of the integrated computational materials engineering. The framework presented is a first step in a through process modelling approach, the prediction of the microstructural features including the maximum pore size. It is the basis for all subsequent modelling steps (e.g. heat treatment, machining and in service performance), and therefore of paramount importance for the fatigue proof design of new cast aluminium components [1].

4. Conclusion

By introducing volume weighted characteristic measures, which describe pore size distributions and relate them to porosity level, it is possible to deduce linear correlations between the mean and maximum equivalent diameter (representing the pores' volumes) as well as mean and maximum envelope diameter (representing the pores' spatial dimensions) and the porosity level. Moreover, it was shown that respective mean and maximum quantities also correlate linearly. Only by weighing the generated XCT results by volume is it possible to make use of XCT data produced using different spatial resolutions and to compensate for differences in microstructural size.

It is remarkable that two characteristic specimen size populations vs. porosity volume are distinguishable, denoted by the grey population (GP) and the black population (BP). It is found that the volume average porosity is the key factor for the development of the mean and maximum pore size distribution measures for both populations. The differences between the populations become apparent only above approximately 0.1% porosity. Both pore size measures and mean and maximum diameters ($d_{s,mean}$, $d_{s,max}$, $d_{e,mean}$ and $d_{e,max}$) exhibit distinctly different linear correlations for the two populations. Both populations consist of high and low Cu containing alloys (app. 2.5 wt-% difference), and differences in Si content (app. 1 wt-% difference). The BP consists of specimen from two different casting processes (Rotacast being a permeant mold process, and CPS being a sand mold process). Moreover, the BP consists of both Na and Sr modified alloys. Interestingly, the modifier, as well as Fe content (high Fe content: Al–8Si–3Cu; low Fe content: Al–7Si–0.5Cu–Mg), cannot be identified as a strong influence on the pore size distribution and its characteristic measures. The effect of eutectic modifier and Fe content

on both the amount of porosity as well as on the pore size distribution could not be established here.

It is shown that sphericity is fundamental in describing the two characteristically different specimen populations arising out of the four alloys, modifications and casting conditions. One population (GP), characterised by low sphericity, has a greater sensitivity of its mean and maximum measures to porosity level when compared to the population characterised by high sphericity pores (BP). It is demonstrated by the calculation of a volume weighted mean sphericity that the pore morphologies of both populations behave differently. It is pointed out that the measures of the pore size distribution can be sufficiently described by the sphericity measure along with the porosity level. For the specimen population exhibiting high sphericity pores, it is observed that mean sphericity appears to reach a constant value above approximately 0.2% porosity. It is proposed that the characteristic difference between the observed pore populations lies in the hydrogen content. To determine the effect of hydrogen regarding the presented analysis method, further experiments need to be conducted.

Finally, it is shown that the knowledge of the local amount of porosity and the mean sphericity are sufficient to predict the local pore size and defect size distribution. The mean sphericity is the key quantity to describe the characteristically different shrinkage driven porosity occurring in the later stages of solidification, and gas driven porosity forming in early stage solidification. Recognition and use of this understanding will enhance the capabilities of integrated computational materials engineering (ICME) approaches significantly.

Disclosure statement

This research is sponsored by MAGMA Gießereitechnologie GmbH and may lead to the development of products which may be licensed to Nematik Linz GmbH, Nematik Dillingen GmbH, or AVL List GmbH. In accordance with Taylor & Francis policy and my ethical obligation as a researcher, I am reporting that I am in the employment of MAGMA Gießereitechnologie GmbH. I have disclosed those interests fully to Taylor & Francis, and have in place an approved plan for managing any potential conflicts arising from this arrangement.

Funding

This work was supported by the Nematik Linz GmbH; Nematik Dillingen GmbH; Materials Center Leoben GmbH; Department of Product Engineering of the Montanuniversität Leoben; AVL List GmbH; Magma Gießereitechnologie GmbH; Austrian Federal Government (Bundesministerium für Verkehr, Innovation und Technologie und Bundesministerium für Wissenschaft, Forschung und Wirtschaft) represented by Österreichische Forschungsgesellschaft mbH; Styrian and the Tyrolean Provincial Government represented by Steirische Wirtschaftsförderungsgesellschaft mbH; and Standortagentur Tirol.

ORCID

M. Weidt  <http://orcid.org/0000-0002-5143-3370>

R. Brunner  <http://orcid.org/0000-0002-0079-3288>

References

- [1] Maijer DM, Gao YX, Lee PD, et al. A through-process model of an A356 brake caliper for fatigue life prediction. *Metall Mater Trans A*. 2004;35:3275–3288.
- [2] Wang QG, Jones PE. Prediction of fatigue performance in aluminum shape castings containing defects. *Metall Mater Trans B*. 2007;38:615–621.
- [3] Murakami Y. *Metal fatigue: effects of small defects and nonmetallic inclusions*. Elsevier; 2002.
- [4] Buffière J-Y, Savelli S, Jouneau P-H, et al. Experimental study of porosity and its relation to fatigue mechanisms of model Al–Si7–Mg0.3 cast Al alloys. *Mater Sci Eng A*. 2001;316:115–126.
- [5] Gao YX, Yi JZ, Lee PD, et al. The effect of porosity on the fatigue life of cast aluminium-silicon alloys. *Fatigue Fract Eng Mater Struct*. 2004;27:559–570.
- [6] Zhang B, Poirier DR, Chen W. Microstructural effects on high-cycle fatigue-crack initiation in A356.2 casting alloy. *Metall Mater Trans A*. 1999;30:2659–2666.
- [7] Couper MJ, Neeson AE, Griffiths JR. Casting defects and the fatigue behaviour of an aluminium casting alloy. *Fatigue Fract Eng Mater Struct*. 1990;13:213–227.
- [8] Garb C, Leitner M, Grün F. Fatigue strength assessment of AlSi7Cu0.5Mg T6W castings supported by computed tomography microporosity analysis. *Procedia Eng*. 2016;160:53–60.
- [9] Wang Q, Apelian D, Lados D. Fatigue behavior of A356/357 aluminum cast alloys. Part II – effect of microstructural constituents. *J Light Met*. 2001;1:85–97.
- [10] Baruchel J, Buffière J-Y, Cloetens P, et al. Advances in synchrotron radiation microtomography. *Scr Mater*. 2006;55:41–46.
- [11] Puncreobutr C, Lee PD, Hamilton RW, et al. Quantitative 3D characterization of solidification structure and defect evolution in Al alloys. *JOM*. 2012;64:89–95.
- [12] Tiedje NS, Taylor JA, Easton MA. A new multi-zone model for porosity distribution in Al–Si alloy castings. *Acta Mater*. 2013;61:3037–3049.
- [13] Dinnis CM, Dahle AK, Taylor JA, et al. The influence of strontium on porosity formation in Al–Si alloys. *Metall Mater Trans A*. 2004;35:3531–3541.
- [14] McDonald SD, Dahle AK, Taylor JA, et al. Modification-related porosity formation in hypoeutectic aluminum-silicon alloys. *Metall Mater Trans B*. 2004;35:1097–1106.
- [15] Li JH, Yang YG, Sömmez S, et al. Simultaneously refining eutectic grain and modifying eutectic Si in Al–10Si–0.3 Mg alloys by Sr and CrB₂ additions. *Int J Cast Met Res*. 2016;29:158–173.
- [16] Savelli S, Buffière JY, Fougères R. Pore characterization in a model cast aluminum alloy and its quantitative relation to fatigue life studied by synchrotron X-ray microtomography. *Mater Sci Forum*. 2000;331–337:197–202.
- [17] Dinnis CM, Taylor JA, Dahle AK. Iron-related porosity in Al–Si–(Cu) foundry alloys. *Mater Sci Eng A*. 2006;425:286–296.
- [18] Taylor JA, Schaffer GB, StJohn DH. The role of iron in the formation of porosity in Al–Si–Cu-based casting alloys: Part I. Initial experimental observations. *Metall Mater Trans A*. 1999;30:1643–1650.

- [19] Taylor JA, Schaffer GB, StJohn DH. The role of iron in the formation of porosity in Al-Si-Cu-based casting alloys: Part II. A phase-diagram approach. *Metall Mater Trans A*. 1999;30:1651–1655.
- [20] Taylor JA, Schaffer GB, StJohn DH. The role of iron in the formation of porosity in Al-Si-Cu-based casting alloys: Part III. A microstructural model. *Metall Mater Trans A*. 1999;30:1657–1662.
- [21] Wang J, Lee PD, Hamilton RW, et al. The kinetics of Fe-rich intermetallic formation in aluminium alloys: in situ observation. *Scr Mater*. 2009;60:516–519.
- [22] Wang J, Li M, Allison J, et al. Multiscale modeling of the influence of Fe content in a Al-Si-Cu alloy on the size distribution of intermetallic phases and micropores. *J Appl Phys*. 2010;107:061804.
- [23] Lee PD, Chirazi A, See D. Modeling microporosity in aluminum-silicon alloys: a review. *J Light Met*. 2001;1:15–30.
- [24] Stefanescu DM. Computer simulation of shrinkage related defects in metal castings – a review. *Int J Cast Met Res*. 2005;18:129–143.
- [25] Carlson KD, Lin Z, Beckermann C. Modeling the effect of finite-rate hydrogen diffusion on porosity formation in aluminum alloys. *Metall Mater Trans B*. 2007;38:541–555.
- [26] Yao L, Cockcroft S, Zhu J, et al. Modeling of microporosity size distribution in aluminum alloy A356. *Metall Mater Trans A*. 2011;42:4137–4148.
- [27] Felberbaum M, Rappaz M. Curvature of micropores in Al-Cu alloys: an X-ray tomography study. *Acta Mater*. 2011;59:6849–6860.
- [28] Garb C, Leitner M, Tauscher M, et al. Statistical analysis of micropore size distributions in Al-Si castings evaluated by X-ray computed tomography. 2017. Manuscript submitted for publication.
- [29] Meishner H, Feikus FJ. Gießverfahren zur Herstellung von Aluminium-Zylinderköpfen und -Zylinderkurbelgehäusen [Casting processes for aluminium cylinder head and crankcase production]. *Giesserei*. 2015;102:34–41. German.
- [30] Oberschelp C, Kirchmeier H, Huber G, et al. Einsatz dynamischer Gießverfahren bei der Herstellung hoch belasteter Zylinderköpfe [Application of dynamic castings processes in highly stressed cylinder heads]. *Giesserei*. 2011;98:26–35. German.
- [31] Amanatiadis A, Andreadis I. A survey on evaluation methods for image interpolation. *Meas Sci Technol*. 2009;20:104015.
- [32] BDG, editor. Volumendefizite von Gussstücken aus Aluminium-, Magnesium- und Zinkgusslegierungen [Volume deficits of aluminium, magnesium, and zinc castings]. BDG; 2010. German.
- [33] Rawle A. Basic principles of particle size analysis. Malvern: Malvern Instruments Limited; p. 8.
- [34] Thiele W. Die Oxydation von Aluminium- und Aluminiumlegierungs-Schmelzen [The oxidation of aluminium and aluminium alloy melts]. 1962. German.
- [35] Mulazimoglu H, Handiak N, Gruzleski JE. Some observations on the reduced pressure test and the hydrogen concentration of modified A356 alloy. *Trans Am Foundrymens Soc*. 1990:225.
- [36] Fredriksson H, Svensson I. On the mechanism of pore formation in metals. *Metall Trans B*. 1976;7:599–606.
- [37] Jones SF, Evans GM, Galvin KP. Bubble nucleation from gas cavities – a review. *Adv Colloid Interface Sci*. 1999;80:27–50.
- [38] Wang J. In-situ observation and mathematical modelling of the nucleation and growth of intermetallics and micropores during the solidification of aluminium alloys. London: Imperial College London; 2009.
- [39] Felberbaum M. Porosity in aluminium alloys: visualization, characterization, and modeling. Lausanne: École Polytechnique Fédérale de Lausanne; 2011.